DECOMPOSITION ASCRIBED SYNERGISTIC LEARNING FOR UNIFIED IMAGE RESTORATION

Anonymous authors
Paper under double-blind review

ABSTRACT

Learning to restore multiple image degradations within a single model is quite beneficial for real-world applications. Nevertheless, existing works typically concentrate on regarding each degradation independently, while their relationship has been less comprehended to ensure the synergistic learning. To this end, we revisit the diverse degradations through the lens of singular value decomposition, with the observation that the decomposed singular vectors and singular values naturally undertake the different types of degradation information, dividing various restoration tasks into two groups, *i.e.*, singular vector dominated and singular value dominated. The above analysis renders a more unified perspective to ascribe diverse degradation connections, compared to previous task-level independent learning. The dedicated optimization of degraded singular vectors and singular values inherently utilizes the potential partnership among diverse restoration tasks, attributing to the Decomposition Ascribed Synergistic Learning (DASL). Specifically, DASL comprises two effective operators, namely, Singular VEctor Operator (SVEO) and Singular VAlue Operator (SVAO), to favor the decomposed optimization, which can be lightly integrated into existing image restoration backbone. Moreover, the congruous decomposition loss has been devised for auxiliary. Extensive experiments on five image restoration tasks demonstrate the effectiveness of our method.

1 INTRODUCTION

Image restoration aims to recover the latent clean images from their degraded observations, and has been widely applied to a series of real-world scenarios, such as photo processing, autopilot, and surveillance. Compared to single-degradation removal Zhou et al. (2021a); Xiao et al. (2022); Qin et al. (2020); Song et al. (2023); Lehtinen et al. (2018); Lee et al. (2022); Pan et al. (2020); Nah et al. (2021); Li et al. (2023); Zhang et al. (2022), the recent flourished multi-degradation learning methods have gathered considerable attention, due to their convenient deployment. However, every rose has its thorn. How to ensure the synergy among diverse restoration tasks demands a dedicated investigation, and it is imperative to comprehend the property of the involved degradations judiciously and include their implicit relationship into consideration.

Generally, existing multi-degradation learning methods concentrated on regarding each degradation independently. For instance, Chen et al. (2021); Li et al. (2020); Valanarasu et al. (2022) propose to deal with different restoration tasks through separate subnetworks or distinct transformer queries. Li et al. (2022); Chen et al. (2022b) propose to distinguish diverse degradation representations via contrastive learning. Remarkably, there are also few attempts devoted to duality degradation removal with synergistic learning. Zhang et al. proposes to leverage the blurry and noisy pairs for joint restoration as their inherent complementarity during digital imaging. Zhou et al. (2022b) proposes a unified network with low-light enhancement encoder and deblurring decoder to address hybrid distortion. Wang et al. (2022a) proposes to quantify the relationship between arbitrary two restoration tasks, and improve the performance of the anchor task with the aid of another task. However, few efforts have been made toward the synergistic learning among more restoration tasks, and there is desperately lacking of a general perspective to comprehend diverse degradations for combing their implicit connections, which set up the stage for this paper.

To solve the above problem, we propose to revisit diverse degradations through the lens of singular value decomposition, and conduct experiments on five common image restoration tasks, including

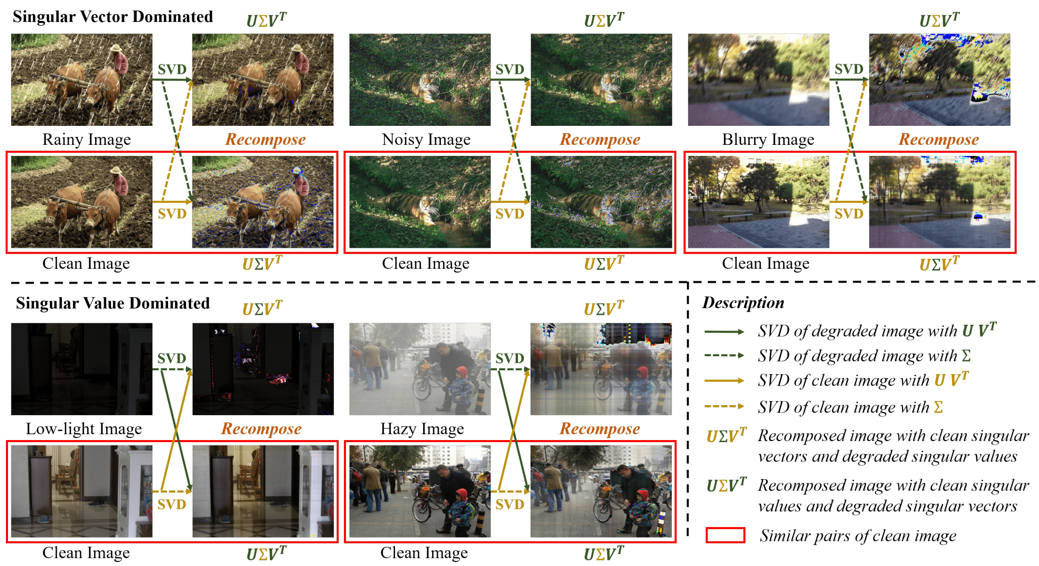

Figure 1: An illustration of the decomposition ascribed analysis on various image restoration tasks through the lens of the singular value decomposition. The decomposed singular vectors and singular values undertake the different types of degradation information as we recompose the degraded image with portions of the clean counterpart, ascribing diverse restoration tasks into two groups, *i.e.*, singular vector dominated *rain, noise, blur*, and singular value dominated *low-light, haze*. Dedicated to the decomposed optimization of the degraded singular vectors and singular values rendering a more unified perspective for synergistic learning, compared to previous task-level independent learning.

image deraining, dehazing, denoising, deblurring, and low-light enhancement. As shown in Fig. 1, it can be observed that the decomposed singular vectors and singular values naturally undertake the different types of degradation information, in that the corruptions fade away when we recompose the degraded image with portions of the clean counterpart. Thus, various restoration tasks can be ascribed into two groups, *i.e.*, singular vector dominated degradations and singular value dominated deagradations. The statistic results in Fig. 2 further validate this phenomenon, where the quantified comparison of the recomposed image quality and singular distribution discrepancy have been presented. Therefore, the potential partnership emerged among diverse restoration tasks could be inherently utilized through the decomposed optimization of singular vectors and singular values, considering their ascribed common properties. Note that more other degradation analyses and theoretical generalization verification are provided in Appendix G.

In this way, we decently convert the previous task-level independent learning into more unified singular vectors and singular values learning, and form our method, Decomposition Ascribed Synergistic Learning (DASL). Basically, one straightforward way to implement our idea is to directly perform the decomposition on latent high-dimensional tensors, and conduct the optimization for decomposed singular vectors and singular values, respectively. However, the huge computational overhead is non-negligible. To this end, two effective operators have been developed to favor the decomposed optimization, namely, Singular VEctor Operator (SVEO) and Singular VAlue Operator (SVAO). Specifically, SVEO takes advantage of the fact that the orthogonal matrices multiplication makes no effect on singular values and only impacts singular vectors, which can be realized through simple regularized convolution layer. SVAO resorts to the signal formation homogeneity between Singular Value Decomposition and the Inverse Discrete Fourier Transform, which can both be regarded as a weighted sum on a set of basis. While the decomposed singular values and the transformed fourier coefficients inherently undertake the same role for linear combination. And the respective base components share similar principle, *i.e.*, from outline to details. Therefore, with approximate derivation, the unattainable singular values optimization can be translated to accessible spectrum maps. We show that the fast fourier transform is substantially faster than the singular value decomposition. Furthermore, the congruous singular decomposition loss has been devised for auxiliary. The proposed DASL can be lightly integrated into existing image restoration backbone for decomposed optimization.

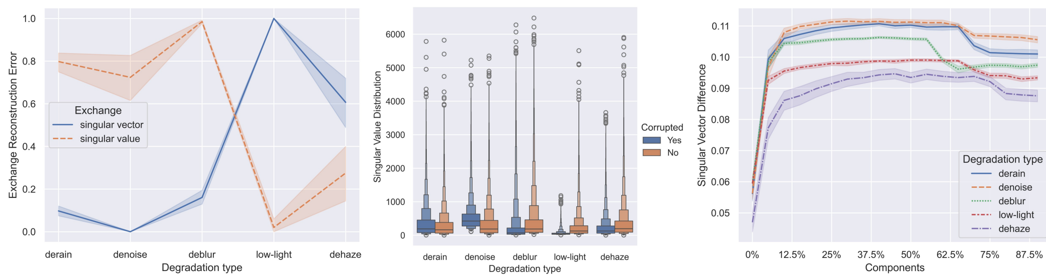

Figure 2: The statistic validation that the decomposed singular vectors and singular values undertake different types of degradation information. (a) The reconstruction error between the recomposed image and paired clean image on five common image restoration tasks. Low error denotes the degradation primarily distributed in the replaced portion of the image. (b) The boxplot comparison of singular value distribution between the degraded image and corresponding clean image, where the singular value dominated *low-light* and *haze* exhibit extraordinary difference. (c) The singular vector difference on separate orders of the component between the degraded image and clean image, where the singular vector dominated *rain*, *noise*, and *blur* present more disparity. The results are obtained under calculation on $\sim$1k images for each restoration task.

The contributions of this work are summarized below:

- We take a step forward to revisit the diverse degradations through the lens of singular value decomposition, and observe that the decomposed singular vectors and singular values naturally undertake the different types of degradation information, ascribing various restoration tasks into two groups, *i.e.*, singular vector dominated and singular value dominated.
- We propose the Decomposition Ascribed Synergistic Learning (DASL) to dedicate the decomposed optimization of degraded singular vectors and singular values respectively, which inherently utilizes the potential partnership among diverse restoration tasks.
- Two effective operators have been developed to favor the decomposed optimization, along with a congruous decomposition loss, which can be lightly integrated into existing image restoration backbone. Extensive experiments on five image restoration tasks demonstrate the effectiveness of our method.

2 Related Work

Image Restoration. Image restoration aims to recover the latent clean images from degraded observations, which has been a long-term problem. Traditional image restoration methods typically concentrated on incorporating various natural image priors along with hand-crafted features for specific degradation removal Babacan et al. (2008); He et al. (2010); Kundur & Hatzinakos (1996). Recently, learning-based methods have made compelling progress on various image restoration tasks, including image denoising Lehtinen et al. (2018); Lee et al. (2022), image deraining Zhou et al. (2021a); Xiao et al. (2022), image deblurring Pan et al. (2020); Nah et al. (2021), image dehazing Zheng et al. (2021); Song et al. (2023), and low-light image enhancement Li et al. (2023); Guo et al. (2020), *etc*. Moreover, numerous general image restoration methods have also been proposed. Zamir et al. (2021; 2022a); Fu et al. (2021) propose the balance between contextual information and spatial details. Mou et al. (2022) formulates the image restoration via proximal mapping for iterative optimization. Zhou et al. (2022a; 2023) proposes to exploit the frequency characteristics to handle diverse degradations. Additionally, various transformer-based methods Zamir et al. (2022b); Liu et al. (2022); Liang et al. (2021); Wang et al. (2022c) have also been investigated, due to their impressive performance in modeling global dependencies and superior adaptability to input contents.

Recently, recovering multiple image degradations within a single model has been coming to the fore, as they are more in line with real-world applications. Zhang et al. proposes to leverage the short-exposure noisy image and the long-exposure blurry image for joint restoration as their inherent complementarity during digital imaging. Zhou et al. (2022b) proposes a unified network to address low-light image enhancement and image deblurring. Furthermore, numerous all-in-one fashion methods Chen et al. (2021); Li et al. (2020; 2022); Valanarasu et al. (2022); Chen et al. (2022b) have been proposed to deal with multiple degradations. Zhang et al. (2023) proposes to correlate various degradations through underlying degradation ingredients. While Park et al. (2023) advocates to separate the diverse degradations propcessing with specific attributed discriminative filters. Besides, most of existing methods concentrated on the network architecture design and few attempts have been made toward exploring the synergy among diverse image restoration tasks.

Tensor Decomposition. Tensor decomposition has been widely applied to a series of fields, such as model compression Jie & Deng (2022); Obukhov et al. (2020), neural rendering Obukhov et al. (2022), multi-task learning Kanakis et al. (2020), and reinforcement learning Sozykin et al.. In terms of image restoration, a large number of decomposition-based methods have been proposed for hyperspectral and multispectral image restoration Peng et al. (2022); Wang et al. (2020; 2017), in that establishing the spatial-spectral correlation with low-rank approximation.

Alternatively, a surge of filter decomposition methods toward networks have also been developed. Zhang et al. (2015); Li et al. (2019); Jaderberg et al. (2014) propose to approximate the original filters with efficient representations to reduce the network parameters and inference time. Kanakis et al. (2020) proposes to reparameterize the convolution operators into a non-trainable shared part and several task-specific parts for multi-task learning. Sun et al. (2022) proposes to decompose the backbone network and only finetune the singular values to preserve the pre-trained semantic clues for few-shot segmentation.

3 Method

In this section, we start with introducing the overall framework of Decomposition Ascribed Synergistic Learning in Section 3.1, and then elaborate the singular vector operator and singular value operator in Section 3.2 and Section 3.3, respectively, which forming our core components. The optimization objective is briefly presented in Section 3.4.

3.1 Overview

The intention of the proposed Decomposition Ascribed Synergistic Learning (DASL) is to dedicate the decomposed optimization of degraded singular vectors and singular values respectively, since they naturally undertake the different types of degradation information as observed in Figs. 1 and 2. And the decomposed optimization renders a more unified perspective to revisit diverse degradations for ascribed synergistic learning. Through examining the singular vector dominated degradations which containing *rain, noise, blur*, and singular value dominated degradations including *hazy, low-light*, we make the following assumptions: (i) The singular vectors responsible for the content information and spatial details. (ii) The singular values represent the global statistical properties of the image. Therefore, the optimization of the degraded singular vectors could be performed throughout the backbone network. And the optimization for the degraded singular values can be condensed to a few of pivotal positions. Specifically, we substitute half of the convolution layers with SVEO, which are uniformly distributed across the entire network. While the SVAOs are only performed at the bottleneck layers of the backbone network. We ensure the compatibility between the optimized singular values and singular vectors through remaining regular layers, and the proposed DASL can be lightly integrated into existing image restoration backbone for decomposed optimization.

3.2 Singular Vector Operator

The singular vector operator is proposed to optimize the degraded singular vectors of the latent representation, and supposed to be decoupled with the optimization of singular values. Explicitly performing the singular value decomposition on high-dimensional tensors solves this problem naturally with little effort, however, the huge computational overhead is non-negligible. Whether can we modify the singular vectors with less computation burden. The answer is affirmative and lies in the orthogonal matrices multiplication.

Theorem 3.1 *For an arbitrary matrix $X \in \mathbb{R}^{h \times w}$ and random orthogonal matrices $P \in \mathbb{R}^{h \times h}, Q \in \mathbb{R}^{w \times w}$, the products of the PX, XQ, PXQ have the same singular values with the matrix X.*

We provide the proof of theorem 3.1 in the Appendix A.1. In order to construct the orthogonal regularized operator to process the latent representation, the form of the convolution operation

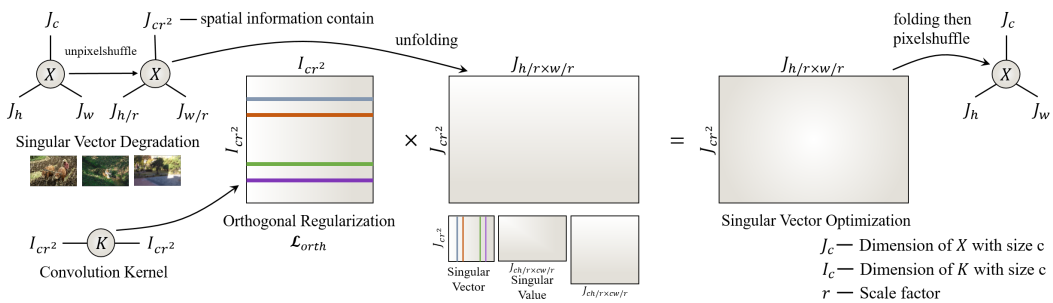

Figure 3: An illustration of the proposed Singular Vector Operator (SVEO), which is dedicated on the optimization of the singular vector dominated degradations, *i.e.*, rain, noise, blur. Theorem 3.1 supports the feasibility and the orthogonal regularization $\mathcal{L}_{orth}$ refers to Eq. 1.

is much eligible than matrix multiplication, which is agnostic to the input resolution. Hence the distinction between these two forms of operation ought to be taken into consideration.

Prior works Sedghi et al. (2019); Jain (1989) have shown that the convolution operation $y = conv(x)$ with kernel size $k \times k$ can be transformed to linear matrix multiplication $vec(y) = A\, vec(x)$. Supposing the processed tensors $y, x \in \mathbb{R}^{1\times n\times n}$ for simplicity, the size of the projection matrix A will come to be $n^2 \times n^2$ with doubly block circulant, which is intolerable to enforce the orthogonal regularization, especially for high-resolution inputs. Another simple way is to employ the 1×1 convolution with regularized orthogonality, however, the singular vectors of the latent representation along the channel dimension will be changed rather than spatial dimension.

Inspired by this point, SVEO proposes to transpose spatial information of the latent representation $X \in \mathbb{R}^{c\times h\times w}$ to channel dimension with the ordinary unpixelshuffle operation Shi et al. (2016), resulting in $X' \in \mathbb{R}^{cr^2\times h/r\times w/r}$. And then applying the orthogonal regularized 1×1 convolution $\mathcal{K} \in \mathbb{R}^{cr^2\times cr^2}$ in this domain, as shown in Fig. 3. Thereby, the degraded singular vectors can be revised pertinently, and the common properties among various singular vector dominated degradations can be implicitly exploited. We note that the differences between SVEO and conventional convolution lie in the following: (i) The SVEO is more consistent with the matrix multiplication as it eliminates the overlap operation attached to the convolution. (ii) The weights of SVEO are reduced to matrix instead of tensor, where the orthogonal regularization can be enforced comfortably. Besides, compared to the matrix multiplication, SVEO further utilizes the channel redundancy and spatial adaptivity within a local $r \times r$ region for conducive information utilization. The orthogonal regularization is formulated as

$$\mathcal{L}_{orth} = \|WW^T \odot (\mathbf{1} - I)\|_F^2, \tag{1}$$

where W represents the weight matrix, $\mathbf{1}$ denotes a matrix with all elements set to 1, and I denotes the identity matrix.

3.3 Singular Value Operator

The singular value operator endeavors to optimize the degraded singular values of the latent representation while supposed to be less entangled with the optimization of singular vectors. However, considering the inherent inaccessibility of the singular values, it is hard to perform the similar operation as SVEO in the same vein. To this end, we instead resort to reconnoitering the essence of singular values and found that it is eminently associated with inverse discrete fourier transform. We provide the formation of a two-dimensional signal represented by singular value decomposition (SVD) and inverse discrete fourier transform (IDFT) in Eq. 2 and Eq. 3 as follows

$$X = U\Sigma V^T = \textstyle\sum_{i=1}^{k} \sigma_i u_i v_i^T = \sum_{i=1}^{k} \sigma_i X_i, \tag{2}$$

where $X \in \mathbb{R}^{h\times w}$ represents the latent representation and $U \in \mathbb{R}^{h\times h}$, $V \in \mathbb{R}^{w\times w}$ represent the decomposed singular vectors with columns u_i, v_i, $k = min(h, w)$ denotes the rank of X. Σ represents the singular values with diagonal elements σ_i.

$$X = \frac{1}{hw}\sum_{u=0}^{h-1}\sum_{v=0}^{w-1} G(u,v)e^{j2\pi(\frac{um}{h}+\frac{vn}{w})} = \frac{1}{hw}\sum_{u=0}^{h-1}\sum_{v=0}^{w-1} G(u,v)\phi(u,v), \tag{3}$$

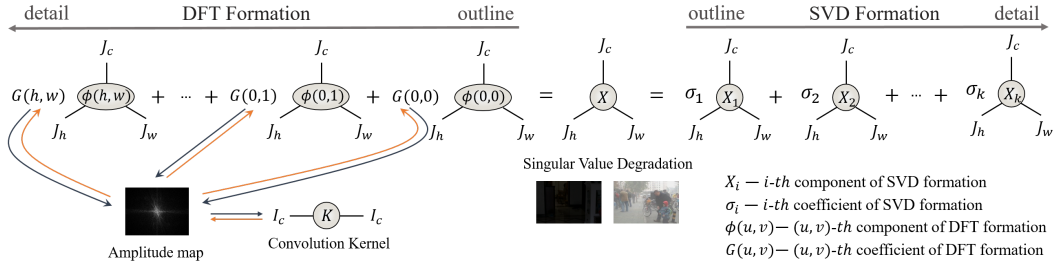

Figure 4: An illustration of the core idea of the proposed Singular Value Operator (SVAO), which is dedicated on the optimization of the singular value dominated degradations, *i.e.*, haze and low-light. Two-dimensional signal formations are provided for simplicity.

where $G(u, v)$ denotes the coefficients of the fourier transform of X, and $\phi(u, v)$ denotes the corresponding two-dimensional wave component. $m \in \mathbb{R}^{h-1}$, $n \in \mathbb{R}^{w-1}$. Observing that both SVD and IDFT formation can be regarded as a weighted sum on a set of basis, *i.e.*, $u_i v_i^T$ and $e^{j2\pi(\frac{um}{h}+\frac{vn}{w})}$, while the decomposed singular values σ_i and the transformed fourier coefficients $G(u, v)$ inherently undertake the same role for the linear combination of various bases.

In Fig. 5, we present the visualized comparison of the reconstruction results using partial components of SVD and IDFT progressively, while both formations conform to the principle from outline to details. Therefore, we presume that the SVD and IDFT operate in a similar way in terms of signal formation, and the combined coefficients σ_i and $G(u, v)$ can be approximated to each other.

Table 1: Time comparison (ms) between SVD and FFT formation for signal representation on high-dimensional tensor, with supposed size $64 \times 128 \times 128$, where the *Decom.* and *Comp.* represent the decomposition and composition.

Formation	*Decom.* time	*Comp.*time	Total time
SVD	180.243	0.143	180.386
FFT	0.159	0.190	0.349

In this way, we successfully translate the unattainable singular values optimization to the accessible fourier coefficients optimization, as shown in Fig. 4. Considering the decomposed singular values typically characterize the global statistics of the signal, SVAO thus concentrates on the optimization of the norm of $G(u, v)$ for consistency, *i.e.*, the amplitude map, since the phase of $G(u, v)$ implicitly represents the structural content Stark (2013); Oppenheim & Lim (1981) and more in line with the singular vectors. The above two-dimensional signal formation can be easily extended to the three-dimensional tensor to perform the 1×1 convolution. Since we adopt the SVAO merely in the bottleneck layers of the backbone network with low resolution inputs, and the fast fourier transform is substantially faster than the singular value decomposition; see Table 1. The consequent overhead of SVAO can be greatly compressed. Note that the formation of Eq. 3 is a bit different from the definitive IDFT, and we provide the equivalence proof in the Appendix A.2.

3.4 Optimization objective

The decomposition loss $\mathcal{L}_{dec}$ is developed to favor the decomposed optimization congruously, formulated as

$$\mathcal{L}_{dec} = \sum_{i=1}^{3} \beta \| U_{rec}^{(i)} V_{rec}^{(i)T} - U_{cle}^{(i)} V_{cle}^{(i)T} \|_1 + \| \Sigma_{rec}^{(i)} - \Sigma_{cle}^{(i)} \|_1, \tag{4}$$

where U_{cle}, V_{cle}, and Σ_{cle} represent the decomposed singular vectors and singular values of the clean image, U_{rec}, V_{rec}, and Σ_{rec} represent the decomposed singular vectors and singular values of the recovered image. For simplicity, we omit the pseudo-identity matrix between UV^T for dimension transformation. β denotes the weight.

The overall optimization objective of DASL comprises the orthogonal regularization loss $\mathcal{L}_{orth}$ and the decomposition loss $\mathcal{L}_{dec}$, together with the original loss functions of the integrated backbone network $\mathcal{L}_{ori}$, formulated as

$$\mathcal{L}_{total} = \mathcal{L}_{ori} + \lambda_{orth} \mathcal{L}_{orth} + \lambda_{dec} \mathcal{L}_{dec}, \tag{5}$$

where λ_{orth} and λ_{dec} denote the balanced weights.

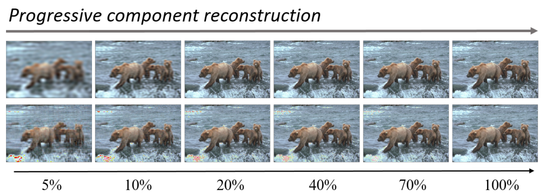

Figure 5: Visual comparison of the progressive reconstruction results with SVD and IDFT components, respectively. First row, IDFT reconstruction result. Second row, SVD reconstruction result. Both conform to the principle from outline to details.

Table 2: Quantitative results on five common image restoration datasets with state-of-the-art general image restoration and all-in-one methods. The baseline results are in grey.

Method	Rain100L		BSD68		GoPro		SOTS		LOL		**Average**		**Params**
	PSNR↑	SSIM↑	PSNR↑	SSIM↑	PSNR↑	SSIM↑	PSNR↑	SSIM↑	PSNR↑	SSIM↑	PSNR↑	SSIM↑	
NAFNet	35.56	0.967	31.02	0.883	26.53	0.808	25.23	0.939	20.49	0.809	27.76	0.881	17.11M
Restormer	34.81	0.962	31.49	0.884	27.22	0.829	24.09	0.927	20.41	0.806	27.60	0.881	26.13M
ShuffleFormer	35.23	0.966	31.53	0.894	27.14	0.828	24.98	0.938	20.12	0.814	27.80	0.888	50.60M
MPRNet	38.16	0.981	31.35	0.889	26.87	0.823	24.27	0.937	20.84	0.824	28.27	0.890	15.74M
DGUNet	36.62	0.971	31.10	0.883	27.25	0.837	24.78	0.940	21.87	0.823	28.32	0.891	17.33M
MambaIR	34.54	0.962	31.37	0.890	26.52	0.804	25.74	0.946	18.23	0.740	27.28	0.868	1.36M
IR-SDE	35.18	0.969	30.26	0.895	25.63	0.777	24.73	0.925	11.83	0.473	25.53	0.808	137.15M
DL	21.96	0.762	23.09	0.745	19.86	0.672	20.54	0.826	19.83	0.712	21.05	0.743	2.09M
Transweather	29.43	0.905	29.00	0.841	25.12	0.757	21.32	0.885	21.21	0.792	25.22	0.836	37.93M
TAPE	29.67	0.904	30.18	0.855	24.47	0.763	22.16	0.861	18.97	0.621	25.09	0.801	1.07M
IDR	35.63	0.965	31.60	0.887	27.87	0.846	25.24	0.943	21.34	0.826	28.34	0.893	15.34M
AirNet	32.98	0.951	30.91	0.882	24.35	0.781	21.04	0.884	18.18	0.735	25.49	0.846	8.93M
PromptIR	34.24	0.957	31.30	0.885	26.43	0.802	25.18	0.934	21.69	0.805	27.76	0.876	35.59M
DA-CLIP	35.69	0.974	30.45	0.898	25.92	0.786	25.24	0.938	17.96	0.738	27.05	0.867	136.82M
DASL+MPRNet	38.02	0.980	31.57	0.890	26.91	0.823	25.82	0.947	20.96	0.826	28.66	0.893	15.15M
DASL+DGUNet	36.96	0.972	31.23	0.885	27.23	0.836	25.33	0.943	21.78	0.824	28.51	0.892	16.92M
DASL+MambaIR	34.82	0.965	31.50	0.892	26.77	0.811	25.89	0.951	19.54	0.775	27.70	0.879	1.02M
DASL+IR-SDE	35.46	0.972	30.43	0.901	25.91	0.789	25.08	0.941	15.26	0.614	26.42	0.843	128.64M
DASL+AirNet	34.93	0.961	30.99	0.883	26.04	0.788	23.64	0.924	20.06	0.805	27.13	0.872	5.41M
DASL+PromptIR	36.67	0.975	31.66	0.896	27.36	0.839	25.55	0.944	21.73	0.834	28.59	0.897	32.31M
DASL+DA-CLIP	35.78	0.979	30.87	0.901	26.08	0.789	25.53	0.947	19.21	0.753	27.49	0.874	130.45M

4 Experiments

In this section, we first clarify the experimental settings, and then present the qualitative and quantitative comparison results with eleven baseline methods for unified image restoration. Moreover, extensive ablation experiments are conducted to verify the effectiveness of our method.

4.1 Implementation Details

Tasks and Metrics. We train our method on five image restoration tasks synchronously. The corresponding training set includes Rain200L Yang et al. (2017) for image deraining, RESIDE-OTS Li et al. (2018) for image dehazing, BSD400 Martin et al. (2001), WED Ma et al. (2016) for image denoising, GoPro Nah et al. (2017) for image deblurring, and LOL Chen et al. (2018) for low-light image enhancement. For evaluation, 100 image pairs in Rain100L Yang et al. (2017), 500 image pairs in SOTS-Outdoor Li et al. (2018), total 192 images in CBSD68 Martin et al. (2001), Urban100 Huang et al. (2015) and Kodak24 Franzen (1999), 1111 image pairs in GoPro Nah et al. (2017), 15 image pairs in LOL Chen et al. (2018) are utilized as the test set. We report the Peak Signal to Noise Ratio (PSNR) and Structural Similarity (SSIM) as numerical metrics.

Training. We implement our method on single NVIDIA Geforce RTX 3090 GPU. For fair comparison, all comparison methods have been retrained in the new mixed dataset with their default hyper parameter settings. We adopt the MPRNet Zamir et al. (2021), DGUNet Mou et al. (2022), and AirNet Li et al. (2022) as our baseline to validate the proposed Decomposition Ascribed Synergistic Learning. The entire network is trained with Adam optimizer for 1200 epochs. We set the batch size as 8 and random crop 128x128 patch from the original image as network input after data augmentation. We set the β in $\mathcal{L}_{dec}$ as 0.01, and the λ_{orth}, λ_{dec} are set to be 1e-4 and 0.1, respectively. We perform evaluations every 20 epochs with the highest average PSNR scores as the final parameters result. More model details and training protocols are presented in the Appendix B.

Table 3: Quantitative results of image denoising on CBSD68, Urban100 and Kodak24 datasets (PSNR↑).

Method	CBSD68 σ=15	CBSD68 σ=25	CBSD68 σ=50	Urban100 σ=15	Urban100 σ=25	Urban100 σ=50	Kodak24 σ=15	Kodak24 σ=25	Kodak24 σ=50
NAFNet	33.67	31.02	27.73	33.14	30.64	27.20	34.27	31.80	28.62
Restormer	34.03	31.49	28.11	33.72	31.26	28.03	34.78	32.37	29.08
MPRNet	34.01	31.35	28.08	34.13	31.75	28.41	34.77	32.31	29.11
DGUNet	33.85	31.10	27.92	33.67	31.27	27.94	34.56	32.10	28.91
MambaIR	33.99	31.37	28.12	34.16	31.83	28.43	34.78	32.38	29.10
IR-SDE	33.23	30.26	26.92	32.31	29.85	26.93	33.82	31.08	27.79
DL	23.16	23.09	22.09	21.10	21.28	20.42	22.63	22.66	21.95
Transweather	31.16	29.00	26.08	29.64	27.97	26.08	31.67	29.64	26.74
TAPE	32.86	30.18	26.63	32.19	29.65	25.87	33.24	30.70	27.19
AirNet	33.49	30.91	27.66	33.16	30.83	27.45	34.14	31.74	28.59
PromptIR	33.92	31.30	28.02	34.06	31.69	28.38	34.63	32.19	29.04
DA-CLIP	33.35	30.45	27.14	32.83	30.24	27.29	34.03	31.26	27.98
DASL+MPRNet	34.16	31.57	28.18	34.21	31.82	28.47	34.91	32.46	29.18
DASL+DGUNet	33.94	31.23	27.94	33.74	31.31	27.96	34.69	32.16	28.93
DASL+MambaIR	34.12	31.50	28.27	34.31	32.04	28.61	35.04	32.64	29.36
DASL+IR-SDE	33.38	30.43	27.09	32.42	29.97	27.05	34.01	31.26	27.95
DASL+AirNet	33.69	30.99	27.68	33.35	30.89	27.46	34.32	31.79	28.61
DASL+PromptIR	34.24	31.66	28.33	34.20	31.84	28.51	34.94	32.41	29.36
DASL+DA-CLIP	33.70	30.87	27.55	33.03	30.47	27.50	34.46	31.67	28.38

Table 4: Evaluating the scalability of decomposed optimization on the full set with merely trained on singular vector dominated degradations (*vec.*) and singular value dominated degradations (*val.*) (PSNR↑).

Tasks	Rain100L	BSD68	GoPro	SOTS	LOL
MPRNet (*vec.*)	39.47	31.50	27.61	15.91	7.77
MPRNet (*val.*)	-	-	-	-	-
DGUNet (*vec.*)	39.04	31.46	28.22	15.92	7.76
DGUNet (*val.*)	23.10	20.39	21.84	24.59	20.45
MambaIR (*vec.*)	37.21	31.53	27.86	16.63	7.76
MambaIR (*val.*)	21.65	20.52	19.67	25.62	21.16
AirNet (*vec.*)	36.62	31.33	26.35	15.90	7.75
AirNet (*val.*)	19.52	19.1	14.47	20.63	16.01
DASL+MPRNet (*vec.*)	39.39	31.63	27.57	17.21	11.23
DASL+MPRNet (*val.*)	21.87	19.96	21.35	25.13	20.33
DASL+DGUNet (*vec.*)	39.11	31.55	28.16	16.87	10.21
DASL+DGUNet (*val.*)	23.19	20.28	22.69	25.05	20.87
DASL+MambaIR (*vec.*)	37.44	31.59	27.92	16.96	9.32
DASL+MambaIR (*val.*)	21.78	20.91	20.35	25.79	21.82
DASL+AirNet (*vec.*)	36.87	31.22	26.72	15.97	8.77
DASL+AirNet (*val.*)	21.25	20.38	21.12	24.60	20.58

4.2 Comparison with state-of-the-art methods

We compare our DASL with comprehensive state-of-the-art methods, including general image restoration methods: NAFNet Chen et al. (2022a), Restormer Zamir et al. (2022b), ShuffleFormer Xiao et al. (2023), MPRNet Zamir et al. (2021), DGUNet Mou et al. (2022),MambaIR Guo et al. (2024), IR-SDE Luo et al. (2023b), and all-in-one fashion methods: DL Fan et al. (2019), Transweather Valanarasu et al. (2022), TAPE Liu et al. (2022), AirNet Li et al. (2022), IDR Zhang et al. (2023), PromptIR Potlapalli et al. (2024), and DA-CLIP Luo et al. (2023a) on five image restoration tasks.

Table 2 reports the quantitative comparison results. It can be observed that the performance of the general image restoration methods is systematically superior to the professional all-in-one methods when more degradations are involved, attributed to the large model size. While our DASL further advances the backbone network capability with fewer parameters, owing to the implicit synergistic learning. We provide more visual comparison results of the DASL integration against the vanilla baselines in Appendix H. Consistent with existing unified image restoration methods Zamir et al. (2022b); Li et al. (2022), we report the detailed denoising results at different noise ratio in Table 3, where the performance gain are consistent.

Table 5: Comparison of the model size and computation complexity between baseline / DASL.

Method	Params (M)	FLOPs (B)	Inference Time (s)
MambaIR	1.36 / 1.02	224.07 / 196.72	1.184 / 1.126
IR-SDE	137.15 / 128.64	1517.34 / 1386.27	18.10 / 17.21
MPRNet	15.74 / 15.15	5575.32 / 2905.14	0.241 / 0.210
DGUNet	17.33 / 16.92	3463.66 / 3020.22	0.397 / 0.391
AirNet	8.93 / 5.41	1205.09 / 767.89	0.459 / 0.190

In Table 5, we present the computation overhead involved in DASL, where the FLOPs and inference time are calculated over 100 testing images with the size of 512×512. It can be observed that our DASL substantially reduces the computation complexity of the baseline methods with considerable inference acceleration, *e.g.*12.86% accelerated on MPRNet and 58.61% accelerated on AirNet. We present the bountiful visual comparison results in the Appendix H, while our DASL exhibits superior visual recovery quality, *i.e.*, more precise details in singular vector dominated degradations and more stable global recovery in singular value dominated degradations.

4.3 Ablation Studies

We present the ablation experiments on the combined degradation dataset with MPRNet as the backbone to verify the effectiveness of our method. In Table 6, we quantitatively evaluate the two developed operators SVEO and SVAO, and the decomposition loss. The metrics are reported on the each of degradations in detail, from which we can make the following observations: **a)** Both SVEO and SVAO are beneficial for advancing the unified degradation restoration performance, attributing to the ascribed synergistic learning. **b)** The congruous decomposition loss is capable to work alone,

Table 6: Ablation experiments on the components design.

Method	*SVEO*	*SVAO*	$\mathcal{L}_{orth}$	$\mathcal{L}_{dec}$	Rain100L PSNR↑	Rain100L SSIM↑	BSD68 PSNR↑	BSD68 SSIM↑	GoPro PSNR↑	GoPro SSIM↑	SOTS PSNR↑	SOTS SSIM↑	LOL PSNR↑	LOL SSIM↑	**Avg.** PSNR↑	**Avg.** SSIM↑
Baseline					38.16	0.981	31.35	0.889	26.87	0.823	24.27	0.937	20.84	0.824	28.27	0.890
With no orth. *SVEO*	✓				37.73	0.981	31.31	0.889	26.79	0.819	24.63	0.939	20.83	0.824	28.26	0.890
With *SVAO*		✓			37.92	0.980	31.41	0.889	26.85	0.821	25.58	0.943	21.05	0.828	28.56	0.892
With *SVEO*	✓		✓		38.04	0.981	31.46	0.890	26.97	0.826	25.53	0.945	20.76	0.822	28.55	0.893
With *SVEO* and *SVAO*	✓	✓	✓		38.01	0.980	31.53	0.890	26.94	0.825	25.63	0.948	20.92	0.826	28.61	0.893
With $\mathcal{L}_{dec}$				✓	38.10	0.982	31.39	0.889	26.78	0.819	24.70	0.942	20.98	0.827	28.39	0.892
DASL+MPRNet	✓	✓	✓	✓	38.02	0.980	31.57	0.890	26.91	0.823	25.82	0.947	20.96	0.826	28.66	0.893

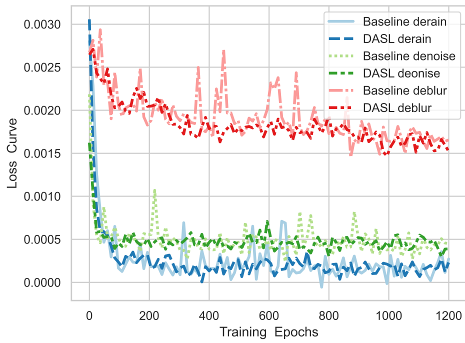

Figure 6: Evaluating the synergy effect through training trajectory between baseline and DASL on *vec.* dominated degradations.

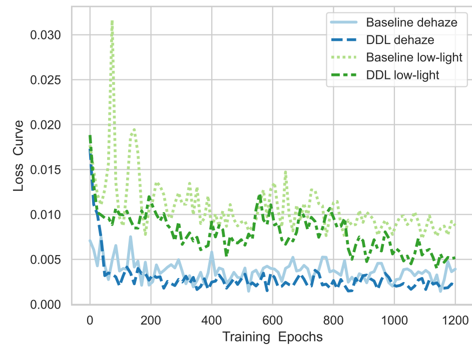

Figure 7: Evaluating the synergy effect through training trajectory between baseline and DASL on *val.* dominated degradations.

and well collaborated with developed operators for decomposed optimization. **c)** The orthogonal regularization is crucial to the reliable optimization of SVEO for preventing the performance drop.

To further verify the scalability of the decomposed optimization, Table 4 evaluates the performance with partially trained on singular vector dominated degradations (*vec.*) and singular value dominated degradations (*val.*). While some properties have been observed: **a)** Basically, the baseline methods concentrate on the trainable degradations, while our DASL further contemplates the untrainable ones in virtue of its slight task dependency. **b)** The performance of MPRNet on *val.* is unattainable due to the non-convergence, however, our DASL successfully circumvents this drawback owing to the more unified decomposed optimization on singular values rather than task-level learning. **c)** The *vec.* seems to be supportive to the restoration performance of *val.*, see the comparison of Tables 2 and 4, indicating the potential relationship among decomposed two types of degradations.

We present the comparison of the training trajectory between baseline and DASL on singular vector dominated and singular value dominated degradations in Figs. 6 and 7. It can be observed that our DASL significantly suppresses the drastic optimization process, retaining the overall steady to better convergence point with even fewer parameters, attributing to the ascribed synergistic learning.

4.4 Latent Space Analysis

The decomposition ascribed degradation analysis has been clearly unveiled in pixel space so far, however, whether the property can be generalized to latent space is more appealing, which is exactly what the DASL built upon for synergestic optimization. In Tab. 7, we provide the validation for latent degradation analysis, where we train a linear projector to transform the degraded latents to clean latents and compute the reconstruction error and transmission ratio Shi et al. (2024). The clean latents are obtained with clean input and extracted from the same layer as degraded latents. To see how well the singular vectors and singular values represent the degradation information, two

Table 7: Validation of the decomposition ascribed degradation analysis in latent space.

Source	Rain100L Loss	Rain100L Ratio	BSD68 Loss	BSD68 Ratio	GoPro Loss	GoPro Ratio	SOTS Loss	SOTS Ratio	LOL Loss	LOL Ratio
Degraded	0.00107	66.1%	0.00143	63.7%	0.00134	55.5%	0.00251	50.1%	0.00943	15.4%
Swap *Vec.*	0.00034	**94.3%**	0.00043	**92.2%**	0.00042	**81.9%**	0.00219	53.1%	0.00926	16.1%
Swap *Val.*	0.00091	70.1%	0.00106	70.8%	0.00129	56.3%	0.00076	**76.8%**	0.00118	**71.2%**
Clean	0.00027	100%	0.00031	100%	0.00019	100%	0.00027	100%	0.00039	100%

variants are conducted with firstly swapping clean singular vectors or singular values to degraded latents, and then perform the linear transformation. The singular vector dominated degradations show noticeable transmission ratio improvement ($\sim$30%) when swapped with clean singular vectors, and exhibit minor transmission ratio improvement ($\sim$5%) when swapped with clean singular values. The same thing also happened in singular value dominated degradations with $\sim$ 25%-50% transmission improvement when swapped with clean singular values and $\sim$3% transmission improvement when swapped with clean singular vectors. Therefore, we have reason to suggest that the latent degradation analysis is consistency with pixel-space degradation analysis in ascribing degradation types.

5 Conclusion

In this paper, we revisited the diverse degradations through the lens of singular value decomposition and observed that the decomposed singular vectors and singular values naturally undertake the different types of degradation information, ascribing various restoration tasks into two groups, *i.e.*, singular vector dominated degradations and singular value dominated degradations. The proposed Decomposition Ascribed Synergistic Learning dedicates the decomposed optimization of degraded singular vectors and singular values respectively, rendering a more unified perspective to inherently utilize the potential partnership among diverse restoration tasks for ascribed synergistic learning. Furthermore, two effective operators SVEO and SVAO have been developed to favor the decomposed optimization, along with a congruous decomposition loss, which can be lightly integrated into existing image restoration backbone. Extensive experiments on bunch of image restoration tasks validated the effectiveness of the proposed method and the generality of the SVD-based degradation analysis.

References

S Derin Babacan, Rafael Molina, and Aggelos K Katsaggelos. Variational bayesian blind deconvolution using a total variation prior. *IEEE Transactions on Image Processing*, 18(1):12–26, 2008.

Hanting Chen, Yunhe Wang, Tianyu Guo, Chang Xu, Yiping Deng, Zhenhua Liu, Siwei Ma, Chunjing Xu, Chao Xu, and Wen Gao. Pre-trained image processing transformer. In *Proceedings of the IEEE/CVF Conference on Computer Vision and Pattern Recognition*, pp. 12299–12310, 2021.

Liangyu Chen, Xiaojie Chu, Xiangyu Zhang, and Jian Sun. Simple baselines for image restoration. In *European Conference on Computer Vision*, pp. 17–33. Springer, 2022a.

Wei Chen, Wang Wenjing, Yang Wenhan, and Liu Jiaying. Deep retinex decomposition for low-light enhancement. In *British Machine Vision Conference*. British Machine Vision Association, 2018.

Wei-Ting Chen, Zhi-Kai Huang, Cheng-Che Tsai, Hao-Hsiang Yang, Jian-Jiun Ding, and Sy-Yen Kuo. Learning multiple adverse weather removal via two-stage knowledge learning and multi-contrastive regularization: Toward a unified model. In *Proceedings of the IEEE/CVF Conference on Computer Vision and Pattern Recognition*, pp. 17653–17662, 2022b.

Qingnan Fan, Dongdong Chen, Lu Yuan, Gang Hua, Nenghai Yu, and Baoquan Chen. A general decoupled learning framework for parameterized image operators. *IEEE transactions on pattern analysis and machine intelligence*, 43(1):33–47, 2019.

Rich Franzen. Kodak lossless true color image suite. *source: http://r0k. us/graphics/kodak*, 4(2), 1999.

Xueyang Fu, Zeyu Xiao, Gang Yang, Aiping Liu, Zhiwei Xiong, et al. Unfolding taylor's approximations for image restoration. *Advances in Neural Information Processing Systems*, 34:18997–19009, 2021.

Chunle Guo, Chongyi Li, Jichang Guo, Chen Change Loy, Junhui Hou, Sam Kwong, and Runmin Cong. Zero-reference deep curve estimation for low-light image enhancement. In *Proceedings of the IEEE/CVF Conference on Computer Vision and Pattern Recognition*, pp. 1780–1789, 2020.

Hang Guo, Jinmin Li, Tao Dai, Zhihao Ouyang, Xudong Ren, and Shu-Tao Xia. Mambair: A simple baseline for image restoration with state-space model. *arXiv preprint arXiv:2402.15648*, 2024.

Kaiming He, Jian Sun, and Xiaoou Tang. Single image haze removal using dark channel prior. *IEEE transactions on pattern analysis and machine intelligence*, 33(12):2341–2353, 2010.

Jia-Bin Huang, Abhishek Singh, and Narendra Ahuja. Single image super-resolution from transformed self-exemplars. In *Proceedings of the IEEE conference on computer vision and pattern recognition*, pp. 5197–5206, 2015.

Max Jaderberg, Andrea Vedaldi, and Andrew Zisserman. Speeding up convolutional neural networks with low rank expansions. *arXiv preprint arXiv:1405.3866*, 2014.

Anil K Jain. *Fundamentals of digital image processing*. Prentice-Hall, Inc., 1989.

Shibo Jie and Zhi-Hong Deng. Fact: Factor-tuning for lightweight adaptation on vision transformer. *arXiv preprint arXiv:2212.03145*, 2022.

Menelaos Kanakis, David Bruggemann, Suman Saha, Stamatios Georgoulis, Anton Obukhov, and Luc Van Gool. Reparameterizing convolutions for incremental multi-task learning without task interference. In *Computer Vision–ECCV 2020: 16th European Conference*, pp. 689–707. Springer, 2020.

Deepa Kundur and Dimitrios Hatzinakos. Blind image deconvolution. *IEEE signal processing magazine*, 13(3):43–64, 1996.

Wooseok Lee, Sanghyun Son, and Kyoung Mu Lee. Ap-bsn: Self-supervised denoising for real-world images via asymmetric pd and blind-spot network. In *Proceedings of the IEEE/CVF Conference on Computer Vision and Pattern Recognition*, pp. 17725–17734, 2022.

Jaakko Lehtinen, Jacob Munkberg, Jon Hasselgren, Samuli Laine, Tero Karras, Miika Aittala, and Timo Aila. Noise2noise: Learning image restoration without clean data. In *International Conference on Machine Learning*, pp. 2965–2974. PMLR, 2018.

Boyi Li, Wenqi Ren, Dengpan Fu, Dacheng Tao, Dan Feng, Wenjun Zeng, and Zhangyang Wang. Benchmarking single-image dehazing and beyond. *IEEE Transactions on Image Processing*, 28 (1):492–505, 2018.

Boyun Li, Xiao Liu, Peng Hu, Zhongqin Wu, Jiancheng Lv, and Xi Peng. All-in-one image restoration for unknown corruption. In *Proceedings of the IEEE/CVF Conference on Computer Vision and Pattern Recognition*, pp. 17452–17462, 2022.

Chongyi Li, Chun-Le Guo, Man Zhou, Zhexin Liang, Shangchen Zhou, Ruicheng Feng, and Chen Change Loy. Embeddingfourier for ultra-high-definition low-light image enhancement. In *ICLR*, 2023.

Ruoteng Li, Robby T Tan, and Loong-Fah Cheong. All in one bad weather removal using architectural search. In *Proceedings of the IEEE/CVF conference on computer vision and pattern recognition*, pp. 3175–3185, 2020.

Yawei Li, Shuhang Gu, Luc Van Gool, and Radu Timofte. Learning filter basis for convolutional neural network compression. In *Proceedings of the IEEE/CVF International Conference on Computer Vision*, pp. 5623–5632, 2019.

Jingyun Liang, Jiezhang Cao, Guolei Sun, Kai Zhang, Luc Van Gool, and Radu Timofte. Swinir: Image restoration using swin transformer. In *Proceedings of the IEEE/CVF International Conference on Computer Vision*, pp. 1833–1844, 2021.

Lin Liu, Lingxi Xie, Xiaopeng Zhang, Shanxin Yuan, Xiangyu Chen, Wengang Zhou, Houqiang Li, and Qi Tian. Tape: Task-agnostic prior embedding for image restoration. In *European Conference on Computer Vision*, pp. 447–464. Springer, 2022.

Ziwei Luo, Fredrik K Gustafsson, Zheng Zhao, Jens Sjölund, and Thomas B Schön. Controlling vision-language models for universal image restoration. *arXiv preprint arXiv:2310.01018*, 3(8), 2023a.

Ziwei Luo, Fredrik K Gustafsson, Zheng Zhao, Jens Sjölund, and Thomas B Schön. Image restoration with mean-reverting stochastic differential equations. In *Proceedings of the 40th International Conference on Machine Learning*, pp. 23045–23066, 2023b.

Kede Ma, Zhengfang Duanmu, Qingbo Wu, Zhou Wang, Hongwei Yong, Hongliang Li, and Lei Zhang. Waterloo exploration database: New challenges for image quality assessment models. *IEEE Transactions on Image Processing*, 26(2):1004–1016, 2016.

David Martin, Charless Fowlkes, Doron Tal, and Jitendra Malik. A database of human segmented natural images and its application to evaluating segmentation algorithms and measuring ecological statistics. In *Proceedings Eighth IEEE International Conference on Computer Vision. ICCV 2001*, volume 2, pp. 416–423. IEEE, 2001.

Chong Mou, Qian Wang, and Jian Zhang. Deep generalized unfolding networks for image restoration. In *Proceedings of the IEEE/CVF Conference on Computer Vision and Pattern Recognition*, pp. 17399–17410, 2022.

Seungjun Nah, Tae Hyun Kim, and Kyoung Mu Lee. Deep multi-scale convolutional neural network for dynamic scene deblurring. In *Proceedings of the IEEE conference on computer vision and pattern recognition*, pp. 3883–3891, 2017.

Seungjun Nah, Sanghyun Son, Suyoung Lee, Radu Timofte, and Kyoung Mu Lee. Ntire 2021 challenge on image deblurring. In *Proceedings of the IEEE/CVF Conference on Computer Vision and Pattern Recognition*, pp. 149–165, 2021.

Anton Obukhov, Maxim Rakhuba, Stamatios Georgoulis, Menelaos Kanakis, Dengxin Dai, and Luc Van Gool. T-basis: a compact representation for neural networks. In *International Conference on Machine Learning*, pp. 7392–7404. PMLR, 2020.

Anton Obukhov, Mikhail Usvyatsov, Christos Sakaridis, Konrad Schindler, and Luc Van Gool. Tt-nf: Tensor train neural fields. *arXiv preprint arXiv:2209.15529*, 2022.

Alan V Oppenheim and Jae S Lim. The importance of phase in signals. *Proceedings of the IEEE*, 69 (5):529–541, 1981.

Jinshan Pan, Haoran Bai, and Jinhui Tang. Cascaded deep video deblurring using temporal sharpness prior. In *Proceedings of the IEEE/CVF Conference on Computer Vision and Pattern Recognition*, pp. 3043–3051, 2020.

Dongwon Park, Byung Hyun Lee, and Se Young Chun. All-in-one image restoration for unknown degradations using adaptive discriminative filters for specific degradations. In *2023 IEEE/CVF Conference on Computer Vision and Pattern Recognition (CVPR)*, pp. 5815–5824. IEEE, 2023.

Jiangjun Peng, Yao Wang, Hongying Zhang, Jianjun Wang, and Deyu Meng. Exact decomposition of joint low rankness and local smoothness plus sparse matrices. *IEEE Transactions on Pattern Analysis and Machine Intelligence*, 2022.

Vaishnav Potlapalli, Syed Waqas Zamir, Salman H Khan, and Fahad Shahbaz Khan. Promptir: Prompting for all-in-one image restoration. *Advances in Neural Information Processing Systems*, 36, 2024.

Xu Qin, Zhilin Wang, Yuanchao Bai, Xiaodong Xie, and Huizhu Jia. Ffa-net: Feature fusion attention network for single image dehazing. In *Proceedings of the AAAI Conference on Artificial Intelligence*, volume 34, pp. 11908–11915, 2020.

Rowayda A Sadek. Svd based image processing applications: State of the art, contributions and research challenges. *International Journal of Advanced Computer Science and Applications*, 3(7), 2012.

Hanie Sedghi, Vineet Gupta, and Philip M. Long. The singular values of convolutional layers. In *International Conference on Learning Representations*, 2019.

Baifeng Shi, Ziyang Wu, Maolin Mao, Xin Wang, and Trevor Darrell. When do we not need larger vision models? *arXiv preprint arXiv:2403.13043*, 2024.

Wenzhe Shi, Jose Caballero, Ferenc Huszár, Johannes Totz, Andrew P Aitken, Rob Bishop, Daniel Rueckert, and Zehan Wang. Real-time single image and video super-resolution using an efficient sub-pixel convolutional neural network. In *Proceedings of the IEEE conference on computer vision and pattern recognition*, 2016.

Yuda Song, Zhuqing He, Hui Qian, and Xin Du. Vision transformers for single image dehazing. *IEEE Transactions on Image Processing*, 32:1927–1941, 2023.

Konstantin Sozykin, Andrei Chertkov, Roman Schutski, ANH-HUY PHAN, Andrzej Cichocki, and Ivan Oseledets. Ttopt: A maximum volume quantized tensor train-based optimization and its application to reinforcement learning. In *Advances in Neural Information Processing Systems*.

Henry Stark. *Image recovery: theory and application*. Elsevier, 2013.

Yanpeng Sun, Qiang Chen, Xiangyu He, Jian Wang, Haocheng Feng, Junyu Han, Errui Ding, Jian Cheng, Zechao Li, and Jingdong Wang. Singular value fine-tuning: Few-shot segmentation requires few-parameters fine-tuning. In *Advances in Neural Information Processing Systems*, 2022.

Jeya Maria Jose Valanarasu, Rajeev Yasarla, and Vishal M Patel. Transweather: Transformer-based restoration of images degraded by adverse weather conditions. In *Proceedings of the IEEE/CVF Conference on Computer Vision and Pattern Recognition*, pp. 2353–2363, 2022.

Kaidong Wang, Yao Wang, Xi-Le Zhao, Jonathan Cheung-Wai Chan, Zongben Xu, and Deyu Meng. Hyperspectral and multispectral image fusion via nonlocal low-rank tensor decomposition and spectral unmixing. *IEEE Transactions on Geoscience and Remote Sensing*, 58(11):7654–7671, 2020.

Wenxin Wang, Boyun Li, Yuanbiao Gou, Peng Hu, and Xi Peng. Relationship quantification of image degradations. *arXiv preprint arXiv:2212.04148*, 2022a.

Yao Wang, Jiangjun Peng, Qian Zhao, Yee Leung, Xi-Le Zhao, and Deyu Meng. Hyperspectral image restoration via total variation regularized low-rank tensor decomposition. *IEEE Journal of Selected Topics in Applied Earth Observations and Remote Sensing*, 11(4):1227–1243, 2017.

Yinhuai Wang, Jiwen Yu, and Jian Zhang. Zero-shot image restoration using denoising diffusion null-space model. In *The Eleventh International Conference on Learning Representations*, 2022b.

Zhendong Wang, Xiaodong Cun, Jianmin Bao, Wengang Zhou, Jianzhuang Liu, and Houqiang Li. Uformer: A general u-shaped transformer for image restoration. In *Proceedings of the IEEE/CVF Conference on Computer Vision and Pattern Recognition*, pp. 17683–17693, 2022c.

Jie Xiao, Xueyang Fu, Aiping Liu, Feng Wu, and Zheng-Jun Zha. Image de-raining transformer. *IEEE Transactions on Pattern Analysis and Machine Intelligence*, 2022.

Jie Xiao, Xueyang Fu, Man Zhou, Hongjian Liu, and Zheng-Jun Zha. Random shuffle transformer for image restoration. In *International Conference on Machine Learning*, pp. 38039–38058. PMLR, 2023.

Wenhan Yang, Robby T Tan, Jiashi Feng, Jiaying Liu, Zongming Guo, and Shuicheng Yan. Deep joint rain detection and removal from a single image. In *Proceedings of the IEEE conference on computer vision and pattern recognition*, pp. 1357–1366, 2017.

SW Zamir, A Arora, SH Khan, H Munawar, FS Khan, MH Yang, and L Shao. Learning enriched features for fast image restoration and enhancement. *IEEE Transactions on Pattern Analysis and Machine Intelligence*, 2022a.

Syed Waqas Zamir, Aditya Arora, Salman Khan, Munawar Hayat, Fahad Shahbaz Khan, Ming-Hsuan Yang, and Ling Shao. Multi-stage progressive image restoration. In *Proceedings of the IEEE/CVF conference on computer vision and pattern recognition*, pp. 14821–14831, 2021.

Syed Waqas Zamir, Aditya Arora, Salman Khan, Munawar Hayat, Fahad Shahbaz Khan, and Ming-Hsuan Yang. Restormer: Efficient transformer for high-resolution image restoration. In *Proceedings of the IEEE/CVF Conference on Computer Vision and Pattern Recognition*, pp. 5728–5739, 2022b.

Jinghao Zhang, Jie Huang, Mingde Yao, Zizheng Yang, Hu Yu, Man Zhou, and Feng Zhao. Ingredient-oriented multi-degradation learning for image restoration. In *Proceedings of the IEEE/CVF Conference on Computer Vision and Pattern Recognition*, pp. 5825–5835, 2023.

Xiangyu Zhang, Jianhua Zou, Kaiming He, and Jian Sun. Accelerating very deep convolutional networks for classification and detection. *IEEE transactions on pattern analysis and machine intelligence*, 38(10):1943–1955, 2015.

Yulun Zhang, Kunpeng Li, Kai Li, Lichen Wang, Bineng Zhong, and Yun Fu. Image super-resolution using very deep residual channel attention networks. In *Proceedings of the European conference on computer vision (ECCV)*, pp. 286–301, 2018.

Zhao Zhang, Suiyi Zhao, Xiaojie Jin, Mingliang Xu, Yi Yang, and Shuicheng Yan. Noiser: Noise is all you need for enhancing low-light images without task-related data. *arXiv preprint arXiv:2211.04700*, 2022.

Zhilu Zhang, RongJian Xu, Ming Liu, Zifei Yan, and Wangmeng Zuo. Self-supervised image restoration with blurry and noisy pairs. In *Advances in Neural Information Processing Systems*.

Zhuoran Zheng, Wenqi Ren, Xiaochun Cao, Xiaobin Hu, Tao Wang, Fenglong Song, and Xiuyi Jia. Ultra-high-definition image dehazing via multi-guided bilateral learning. In *2021 IEEE/CVF Conference on Computer Vision and Pattern Recognition (CVPR)*, pp. 16180–16189. IEEE, 2021.

Man Zhou, Jie Xiao, Yifan Chang, Xueyang Fu, Aiping Liu, Jinshan Pan, and Zheng-Jun Zha. Image de-raining via continual learning. In *Proceedings of the IEEE/CVF Conference on Computer Vision and Pattern Recognition*, pp. 4907–4916, 2021a.

Man Zhou, Hu Yu, Jie Huang, Feng Zhao, Jinwei Gu, Chen Change Loy, Deyu Meng, and Chongyi Li. Deep fourier up-sampling. In *Advances in Neural Information Processing Systems*, 2022a.

Man Zhou, Jie Huang, Chun-Le Guo, and Chongyi Li. Fourmer: An efficient global modeling paradigm for image restoration. In *International Conference on Machine Learning*, pp. 42589–42601. PMLR, 2023.

Shangchen Zhou, Chongyi Li, and Chen Change Loy. Lednet: Joint low-light enhancement and deblurring in the dark. In *Computer Vision–ECCV 2022: 17th European Conference, Tel Aviv, Israel, October 23–27, 2022, Proceedings, Part VI*, pp. 573–589. Springer, 2022b.

Yuqian Zhou, David Ren, Neil Emerton, Sehoon Lim, and Timothy Large. Image restoration for under-display camera. In *Proceedings of the IEEE/CVF Conference on Computer Vision and Pattern Recognition*, pp. 9179–9188, 2021b.

A Proof of the Propositions

A.1 Proof of Theorem 1

Theorem A.1 *For an arbitrary matrix $X \in \mathbb{R}^{h\times w}$ and random orthogonal matrices $P \in \mathbb{R}^{h\times h}, Q \in \mathbb{R}^{w\times w}$, the products of the PX, XQ, PXQ have the same singular values with the matrix X.*

Proof. According to the definition of Singular Value Decomposition (SVD), we can decompose matrix $X \in \mathbb{R}^{h\times w}$ into USV^T, where $U \in \mathbb{R}^{h\times h}$ and $V \in \mathbb{R}^{w\times w}$ indicate the orthogonal singular vector matrices, $S \in \mathbb{R}^{h\times w}$ indicates the diagonal singular value matrix. Thus $X^{'}$=PXQ=$PUSV^TQ$. Denotes $U^{'}$=PU and $V^{'T}$=V^TQ, then $X^{'}$ can be decomposed into $U^{'}SV^{'T}$ if $U^{'}$ and $V^{'T}$ are orthogonal matrices.

$$U^{'-1} = (PU)^{-1} = U^{-1}P^{-1} = U^TP^T = (PU)^T = U^{'T} \tag{6}$$

$$(V^{'T})^{-1} = (V^TQ)^{-1} = Q^{-1}(V^T)^{-1} = Q^TV = (V^TQ)^T = V^{'} \tag{7}$$

Therefore, $U^{'}U^{'T} = I$ and $V^{'T}V^{'} = I$, where I denotes the identity matrix, and $U^{'}$, $V^{'T}$ are orthogonal. $X^{'}$ and X have the same singular values S, and the singular vectors of X can be orthogonally transformed to PU, Q^TV. Correspondingly, it can be easily extended to the case of PX and XQ. □

A.2 Equivalence Proof of Equation 3 and IDFT

Proposition. *The signal formation principle in Equation 3 is equivalence to the definitive Inverse Discrete Fourier Transform (IDFT), where we restate the Equation 3 as following:*

$$X = \frac{1}{hw}\sum_{u=0}^{h-1}\sum_{v=0}^{w-1} G(u,v)e^{j2\pi(\frac{um}{h}+\frac{vn}{w})},\ m \in \mathbb{R}^{h-1}, n \in \mathbb{R}^{w-1}. \tag{8}$$

Proof. For the two-dimensional signal $X \in \mathbb{R}^{h\times w}$, we can represent any point on it through IDFT. Supposing (m,n) and ($m^{'}$, $n^{'}$) are two random points on X, where m, $m^{'}$ ∈ [0, h-1], n, $n^{'}$ ∈ [0, w-1], and (m,n) ≠ ($m^{'}$, $n^{'}$), we have

$$X(m,n) = \frac{1}{hw}\sum_{u=0}^{h-1}\sum_{v=0}^{w-1} G(u,v)e^{j2\pi(\frac{um}{h}+\frac{vn}{w})}, \tag{9}$$

$$X(m^{'},n^{'}) = \frac{1}{hw}\sum_{u=0}^{h-1}\sum_{v=0}^{w-1} G(u,v)e^{j2\pi(\frac{um^{'}}{h}+\frac{vn^{'}}{w})}. \tag{10}$$

$X(m,n)$ represents the signal value at (m,n) position on X, and the same as $X(m^{'},n^{'})$. Thus, we can rewrite X as

$$\begin{aligned} X &= \begin{bmatrix} X(0,0) & \cdots & X(0,w-1) \\ \vdots & \ddots & \vdots \\ X(h-1,0) & \cdots & X(h-1,w-1) \end{bmatrix} \\ &= \frac{1}{hw}\sum_{u=0}^{h-1}\sum_{v=0}^{w-1} G(u,v) \cdot \begin{bmatrix} e^{j2\pi(\frac{u0}{h}+\frac{v0}{w})} & \cdots & e^{j2\pi(\frac{u0}{h}+\frac{v(w-1)}{w})} \\ \vdots & \ddots & \vdots \\ e^{j2\pi(\frac{u(h-1)}{h}+\frac{v0}{w})} & \cdots & e^{j2\pi(\frac{u(h-1)}{h}+\frac{v(w-1)}{w})} \end{bmatrix} \\ &= \frac{1}{hw}\sum_{u=0}^{h-1}\sum_{v=0}^{w-1} G(u,v)e^{j2\pi(\frac{um}{h}+\frac{vn}{w})}, \end{aligned} \tag{11}$$

where $m \in \mathbb{R}^{h-1}, n \in \mathbb{R}^{w-1}$. And the two-dimensional wave $e^{j2\pi(\frac{um}{h}+\frac{vn}{w})} \in \mathbb{R}^{h-1 \times w-1}$ denotes the base component. Therefore, the formation principle of Eq 3 is equivalent to the definitive IDFT, *i.e.*, Eqs 9 and 10. $\square$

B Model details and Training Protocols

We implement our DASL with integrated MPRNet Zamir et al. (2021), DGUNet Mou et al. (2022), and AirNet Li et al. (2022) backbone to validate the effectiveness of the decomposed optimization. All experiments are conducted using PyTorch, with model details and training protocols provided in Table 8. Fig. 8 (a) presents the compound working flow of our operator. Note that the SVAO is only adopted in the bottleneck layer, as described in Section 3.1. We introduce how we embed our operator into the backbone network from a microscopic perspective. Sincerely, the most convenient way is to directly reform the basic block of the backbone network. We present two fashions of the basic block of baseline in Fig. 8 (b) and (c), where the MPRNet fashion is composed of two basic units, *e.g.*, channel attention block (CAB) Zhang et al. (2018), and DGUNet is constructed by two vanilla activated convolutions. We simply replace one of them (dashed line) with our operator to realize the DASL integration. Note that AirNet shares the similar fashion as MPRNet.

Table 8: Model details and training protocols for DASL integrated baselines.

Configurations	MPRNet	DGUNet	AirNet
optimizer	Adam	Adam	Adam
base learning rate	2e-4	1e-4	1e-3
learning rate schedular	Cosine decay	Cosine decay	Linear decay
momentum of Adam	$\beta_1 = 0.9, \beta_2 = 0.999$	$\beta_1 = 0.9, \beta_2 = 0.999$	$\beta_1 = 0.9, \beta_2 = 0.99$
channel dimension	80	80	256
augmentation	RandomCropFlip	RandomCropFlip	RandomCropFlip
num. of replaced operator	18	14	50
basic block	channel attention block	activated convolution	degradation guided module
optimization objective	CharbonnierLoss + EdgeLoss	CharbonnierLoss + EdgeLoss	L1Loss

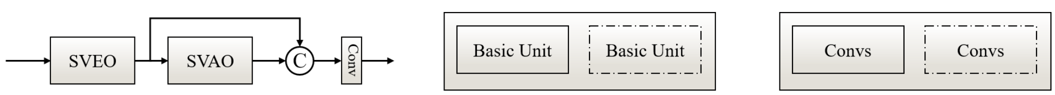

(a) Our operator (b) MPRNet fashion (c) DGUNet fashion

Figure 8: The strategy of model integration with DASL. (a) The working flow of our operator. (b) The basic building block of MPRNet fashion. (c) The basic building block of DGUNet fashion.

C Trivial Ablations on operator design

The ablation experiment on the choice of scale factor r in SVEO is provided in Table 9. Note that the larger r will incur larger model size. We empirically set the scale ratio r in SVEO as 2. The working flow ablation of combined operator is provided in Table 10, and the compound fashion is preferred.

Table 9: Ablation experiments on the scale ratio r in the SVEO (PSNR↑).

Scale ratio	Rain100L	SOTS	GoPro	BSD68	LOL
1	38.01	31.55	26.88	25.84	20.93
2	38.02	31.57	26.91	25.82	20.96
4	38.07	31.58	26.92	25.81	20.98

Table 10: Ablation experiments on the working flow of the combined operator (PSNR↑).

Working flow	Rain100L	SOTS	GoPro	BSD68	LOL
cascaded	38.01	31.55	26.88	25.84	20.87
parallel	38.02	31.57	26.91	25.82	20.88
cascaded + parallel	38.02	31.57	26.91	25.82	20.96

D Extension experiments for property validation

In Table 11, we provide the performance of DASL on real-world image restoration tasks, *i.e.*, under-display camera (UDC) image enhancement. Typically, images captured under UDC system suffer from both blurring due to the spread point spread function, and lower light transmission rate.

Compared to vanilla baseline models, DASL is capable of boosting the performance consistently. Note that the above experiments are performed on real-world UDC dataset Zhou et al. (2021b) without any fine-tuning, validating the capability of the model for processing undesirable degradations. Table 12 evaluates the potential of DASL integration on transformer-based image restoration backbone. Albeit the convolutional form of the developed decomposed operators, the supposed architecture incompatibility problem is not come to be an obstacle. Note that we replace the projection layer at the end of the attention mechanism with developed operators for transformer-based methods.

Table 11: Quantitative results of real-world image restoration tasks (under-display camera image enhancement) on TOLED and POLED datasets.

Method	TOLED			POLED		
	PSNR↑	SSIM↑	LPIPS↓	PSNR↑	SSIM↑	LPIPS↓
MPRNet	24.69	0.707	0.347	8.34	0.365	0.798
DGUNet	19.67	0.627	0.384	8.88	0.391	0.810
AirNet	14.58	0.609	0.445	7.53	0.350	0.820
DASL+MPRNet	25.65	0.733	0.326	8.95	0.392	0.788
DASL+DGUNet	25.25	0.727	0.329	9.80	0.410	0.783
DASL+AirNet	18.83	0.637	0.426	9.13	0.398	0.784

Table 12: Evaluating the generality of the DASL integration on transformer-based image restoration backbone among five common image restoration tasks (PSNR↑).

Methods	Rain100L	BSD68	GoPro	SOTS	LOL
SwinIR	30.78	30.59	24.52	21.50	17.81
Restormer	34.81	31.49	27.22	24.09	20.41
ShuffleFormer	35.23	31.53	27.14	24.98	20.12
DASL+SwinIR	33.53	30.84	25.72	24.10	20.36
DASL+Restormer	35.79	31.67	27.35	25.90	21.39
DASL+ShuffleFormer	35.92	31.59	27.44	25.08	20.18

E Cultivating the SVD potential for image restoration.

In fact, Singular Value Decomposition (SVD) has been widely applied for a range of image restoration tasks, such as image denoising, image compression, etc., attributing to the attractive rank properties Sadek (2012) including *truncated energy maximization* and *orthogonal subspaces projection*. The former takes the fact that SVD provides the optima low rank approximation of the signal in terms of dominant energy preservation, which could greatly benefit the signal compression. The latter exploits the fact that the separate order of SVD-decomposed components are orthogonal, which inherently partition the signal into independent rank space, e.g., signal and noise space or range and null space for further manipulation, supporting the application of image denoising or even prevailing inverse problem solvers Wang et al. (2022b). Moreover, the SVD-based degradation analysis proposed in this work excavates another promising property of SVD from the vector-value perspective, which is essentially different from previous rank-based method. Encouragingly, the above two perspectives have the potential to collaborate well and the separate order property is supposed to be incorporated into the DASL for sophisticated degradation relationship investigation in future works. We note that the above two SVD perspectives have the opportunity to collaborate well and the separate order potential is supposed to be incorporated into the DASL for sophisticated relationship investigation in future works.

F Broader Impact

This work potentially release the redundant model deployments in real world scenarios, and sincerely benefits a lot of edge applications with limited resources, such as mobile photography and 24/7 surveillance. The privacy of our method may raise potential concerns when considering the removal of some important occlusions in the original images, resulting in the disclosure of private information. Therefore, how to ensure the user-agnostic security of our method needs further investment.

G More degradation analysis and generalizable verification

We provide more visual results of decomposition ascribed analysis for diverse degradations in Figs. 11 and 12, to further verify our observation that the decomposed singular vectors and singular values naturally undertake the different types of degradation information. In Figs. 10 and 13, we provide more degradation analysis to validate the generality of the proposed decomposition ascribed analysis, including *downsampling, compression, color shifting, underwater enhancement, and sandstorm enhancement*. The former three types are ascribed into singular vector dominated degradations and the latter two types are ascribed into singular value dominated degradations.

Experimentally, if we reexamine the two groups of degradation through SVD-ascribed analysis, namely, *rain, noise, blur, downsampling, compression, color shifting* in singular vector dominated and *hazy, low-light, underwater enhancement, sandstorm enhancement* in singular value dominated,

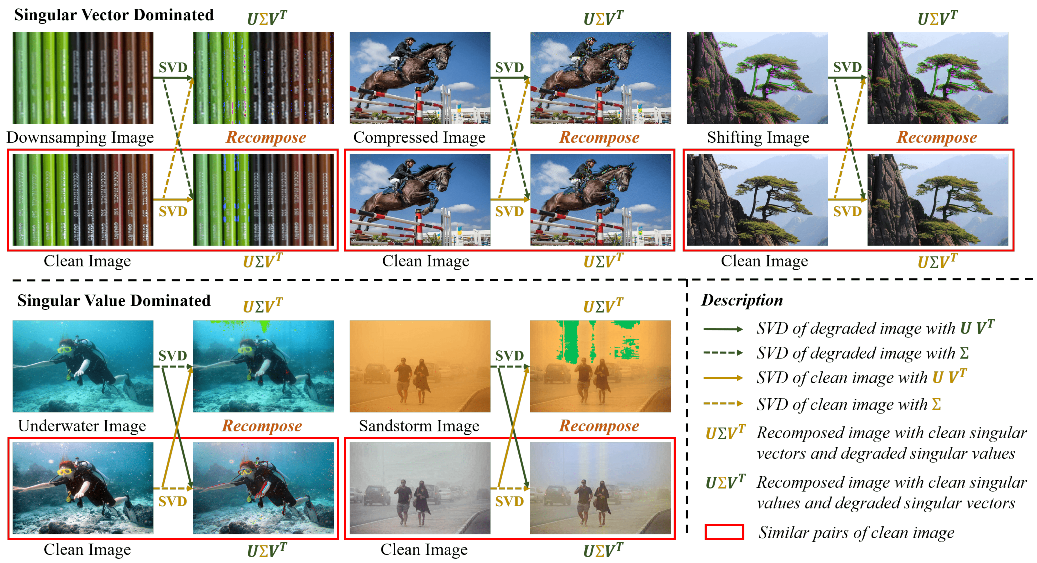

Figure 9: An illustration of the decomposition ascribed degradation analysis on various image restoration tasks through the lens of the singular value decomposition.

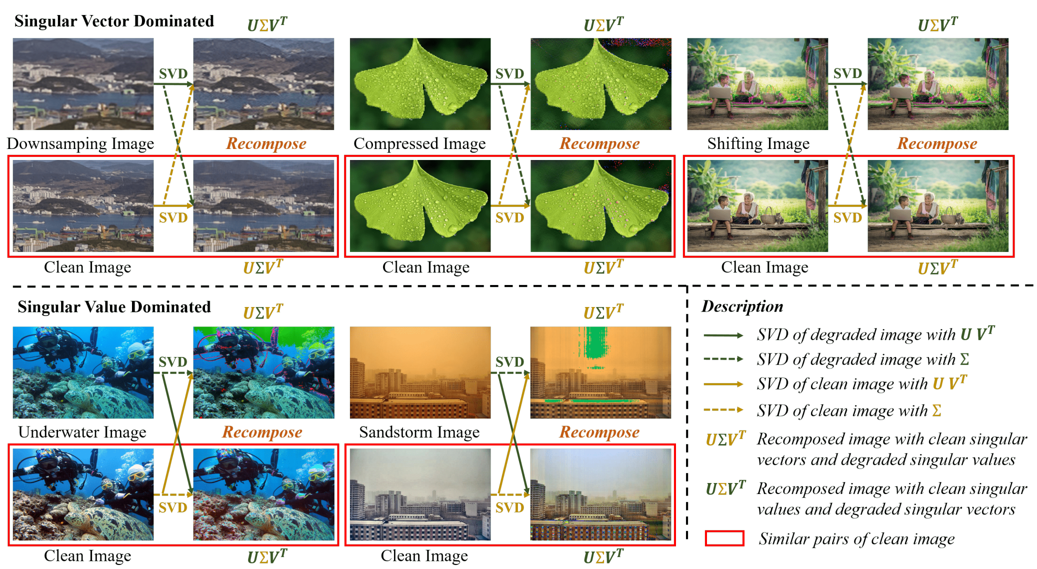

Figure 10: An illustration of the decomposition ascribed degradation analysis on various image restoration tasks through the lens of the singular value decomposition.

it can be concluded that the singular vectors responsible for the spatial content information, while the singular values represent the statistical properties of the image.

Theoretically, we verify the above conjecture from the signal formation perspective of SVD, where any signal can be regarded as a weighted sum on a set of basis, i.e., $X = U\Sigma V^T = \sum_{i=1}^{k} \sigma_i u_i v_i^T$. In this light, the singular vectors $\cup_{i=1}^{k}\{u_i v_i^T\}$ represent the base components of the signal for content composition, and the singular values $\cup_{i=1}^{k}\{\sigma_i\}$ represent the combined coefficients for statistical modulation. Their respective dominated degradation types are fundamentally determined by such signal formation properties, i.e., content corruption and statistic distortion. Owing to the closed form of the signal formation principle of SVD, the decomposition ascribed degradation analysis is theoretically generalizable to most of scenes.

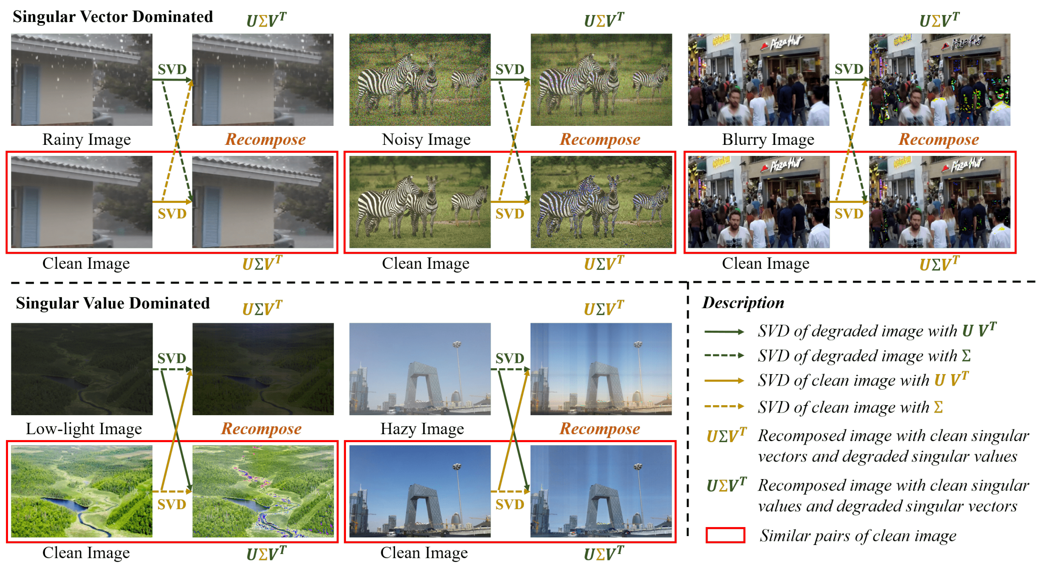

Figure 11: An illustration of the decomposition ascribed degradation analysis on various image restoration tasks through the lens of the singular value decomposition.

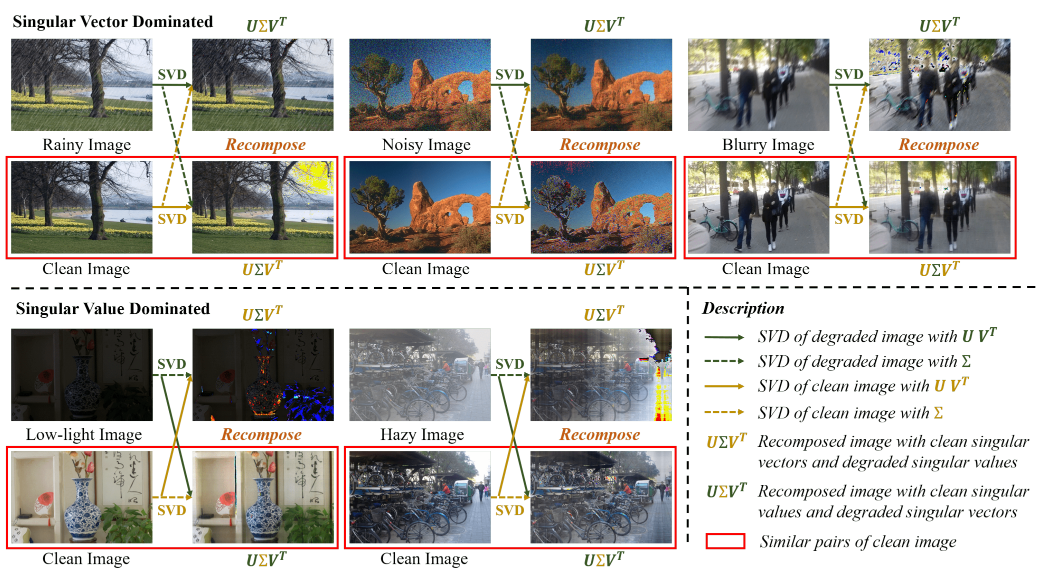

Figure 12: An illustration of the decomposition ascribed degradation analysis on various image restoration tasks through the lens of the singular value decomposition.

H Visual comparison results

We present the visual comparison results of the aforementioned image restoration tasks in Figs. 14 to 18, including singular vector dominated degradations *rain*, *noise*, *blur*, and singular value dominated degradations *low-light*, *haze*. It can be observed that our DASL exhibits superior visual recovery quality in both types of degradation, *i.e.*, more precise content details in singular vector dominated degradations and more stable global recovery in singular value dominated degradations, compared to the integrated baseline method.

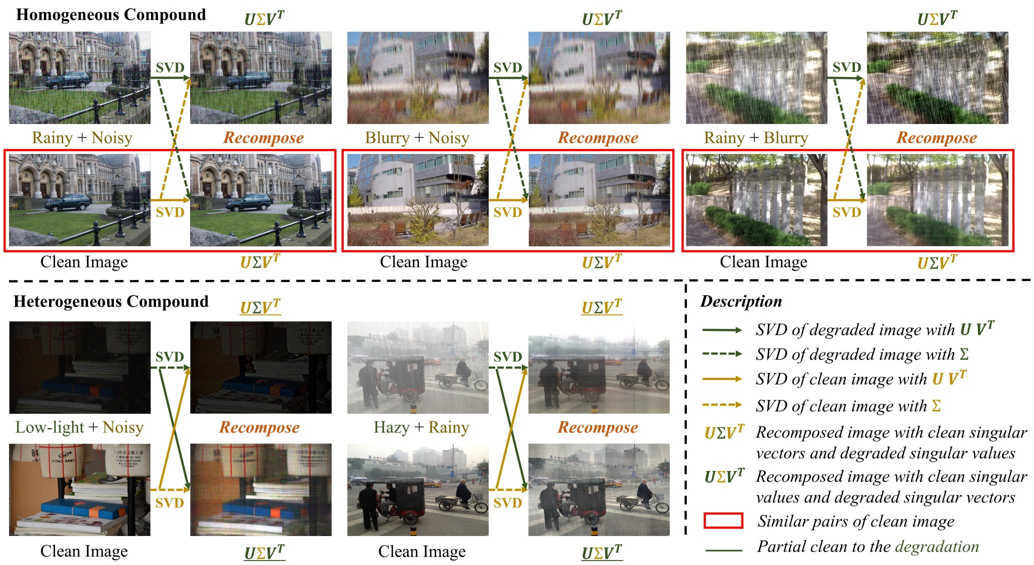

Figure 13: An illustration of the decomposition ascribed degradation analysis on compound degradations, where the pre-ascribed singular vector dominated degradations and singular value dominated degradations are marked. The homogeneous compound degradations refer to that both degradations are ascribed at one side of singular vectors or singular values, and the heterogeneous compound degradations refer to that the degradations are ascribed at both side of singular vectors and singular values, and is consistent with ascription in single degradation analysis.

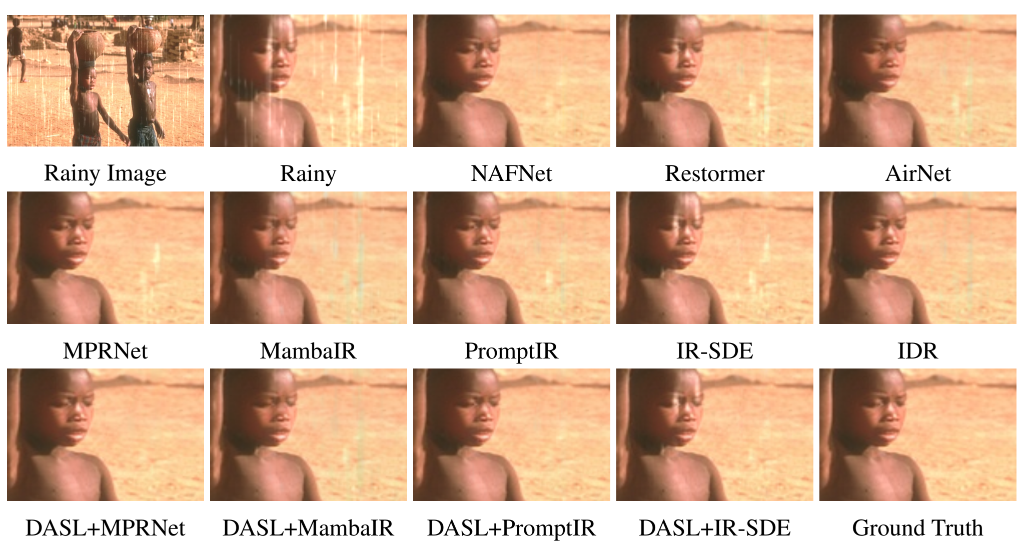

Figure 14: Visual comparison with state-of-the-art methods on Rain100L dataset.

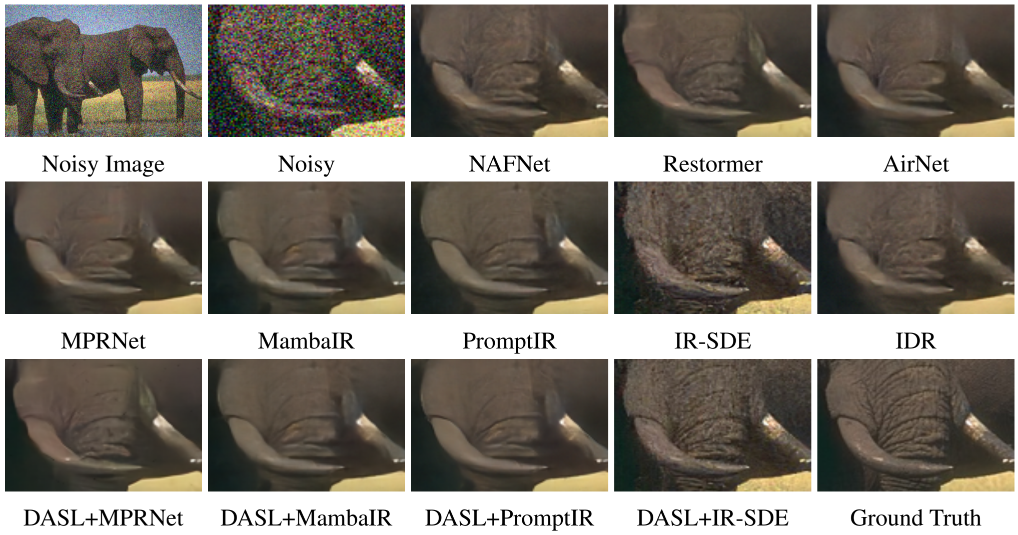

Figure 15: Visual comparison with state-of-the-art methods on BSD68 dataset.

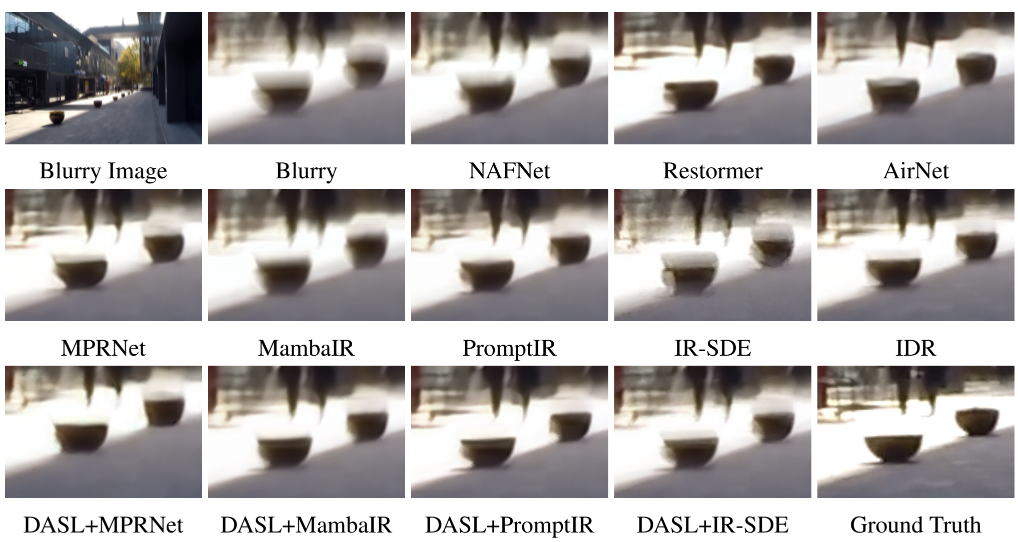

Figure 16: Visual comparison with state-of-the-art methods on GoPro dataset.

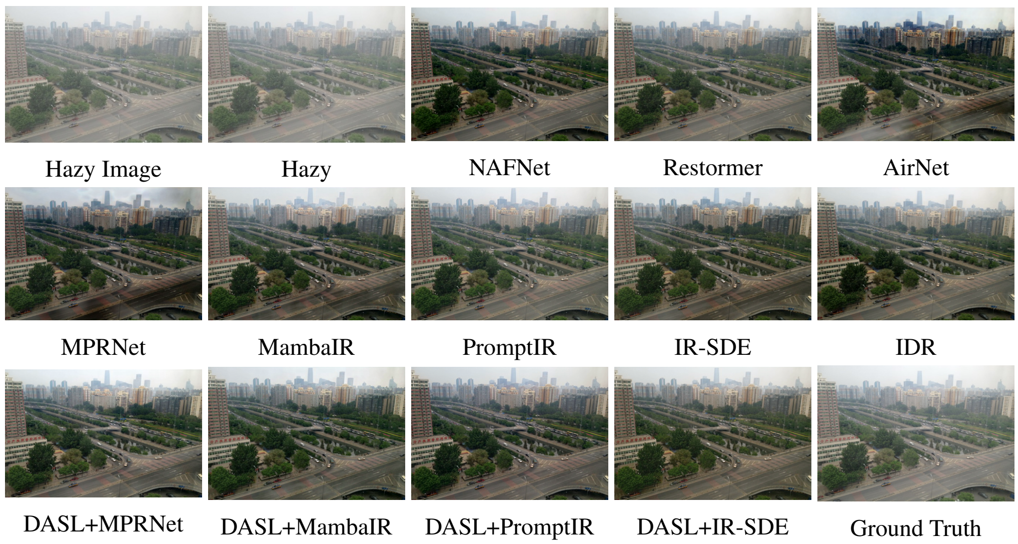

Figure 17: Visual comparison with state-of-the-art methods on SOTS dataset.

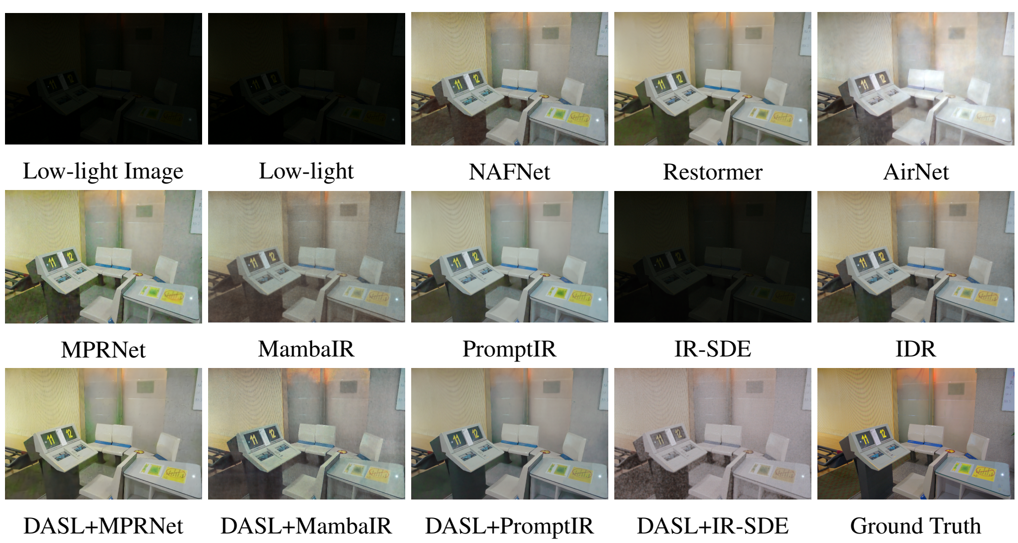

Figure 18: Visual comparison with state-of-the-art methods on LOL dataset.